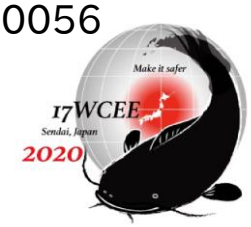

17th World Conference on Earthquake Engineering, 17WCEE

Sendai, Japan - September 13th to 18th 2020

SIMULATE REINFORCEMENT DUCTILE FRACTURE IN CONCRETE STRUCTURES UNDER EARTHQUAKS

K. Zhong[(1)], G. G. Deierlein[(2)]

[(1)] *Ph.D. student, Department of Civil and Environmental Engineering, Stanford University, kuanshi@stanford.edu*
[(2)] *John A. Blume Professor, Department of Civil and Environmental Engineering, Stanford University, ggd@stanford.edu*

Abstract

Reinforcement fracture is a critical failure mode that may cause the instability of concrete members and subsequent global failure under earthquake loads. This paper introduces a new ductile fracture model that is capable of simulating the reinforcement fracture. The proposed model quantifies the cumulative damage by the fracture index (*FI*) which is computed from the plastic strain and stress triaxiality history at the fracture loci.

The state-of-the-art fatigue-fracture method is briefly reviewed, and its limitations are discussed. Then, the detailed finite element models and fiber models are used to simulate the local strain-stress field, based on which the void-growth coefficient, symmetric coefficient, and cyclic deterioration coefficient are calibrated such that the resulting *FI* equals to 1.0 at the failure points in available monotonic and cyclic tests. To facilitate the application of the proposed model in fiber element analysis to capture reinforcement failure in reinforced concrete members, two closed-form solutions for local strain demands with necking-induced and buckling induced strain localizations are developed, i.e., Necking Amplification Model (NAM) and Buckling Adjustment Model (BAM). Both models are calibrated and verified for converting the gauge strain-stress histories to the local strain-stress histories.

The proposed ductile fracture model is also implanted in OpenSees as a new uniaxial material to simulate the stiffness degradation and strength loss of reinforced concrete members due to reinforcement fracture. A validation study is presented in which the observed reinforcement ruptures in one shake-table bridge column test can be accurately simulated by using the new uniaxial material in the fiber element analysis. A case study is also presented to (1) demonstrate the importance of simulating the reinforcement bar fracture for assessing the seismic performance of reinforced concrete bridge columns; and (2) the efficacy of the new ductile fracture model and the new uniaxial material. One archetype single-column-bent bridge is modeled using the calibrated fiber element approach. The incremental dynamic analysis (IDA) is conducted to develop the analytical fragility functions for different curvature-based damage states as well as the structural collapse fragility. Then, the analysis is repeated for the same bridge model but without using the new fracture material, where the median Sa's of damage states and the median collapse capacity are found to be overestimated.

Keywords: reinforcement; ductile fracture; necking; buckle; fragility

1. Introduction

Reinforcement fracture is a critical failure mode that may cause the instability of concrete members and subsequent global failure under earthquake loads. The global stress and strain responses (so-called the gauge stress and strain) are commonly used in predicting catastrophic failure. The number of cycles before the material failure was found to be dependent on the stress amplitude [1, 2]. The concept that the cyclic fatigue life relies on the strain range was proposed to address the dilemma that the measured stress range is not a reliable measure in cyclic strain-hardening/softening material [3]. The strain-based model is built on the assumption that the threshold of irreversible damage is proportional to the amplitude of plastic strain in a log-log linear manner. Its accuracy has been verified and improved by many subsequent investigations [4, 5] for the low-cycle fatigue problem with 10^2 to 10^5 half cycles [6]. The mean stress and strain effects on the high-cycle fatigue failure were studied to correct the prediction bias under the asymmetric loading history [7, 8]. The rain-flow counting method was developed to count the equivalent half-cycle amplitudes in the random loading history [9, 10].

More recently, researches were conducted to use the strain-based model for evaluating the cyclic strain life of reinforcement. Mander et al. [11] studied the low-cycle fatigue behavior of A615 grade 40 and A722 pre-stressing reinforcement with different slenderness ratios or strain ranges. While validating the existing fatigue models at that time (e.g., Coffin-Manson model), a series of hysterical-energy fatigue models were proposed and calibrated to their test results. It was noted that the mean stress and mean strain were found to have negligible effects in experiments. It was also found that the cycling can continue after the incipient failure (first cracking) and the crack would propagate causing strength deterioration until the rupture occurs (defined by the significant in-cycle degradation of force capacity). Brown and Kunnath [12] conducted an experimental study including 34 constant amplitude fatigue tests with bar sizes from #6 (#19 in metric) to #8 (#25 in metric). Fatigue cracks were observed to initiate at the base of the rolled-on deformations and then propagate in both directions. They also found that the bar buckling can reduce the fatigue life of reinforcement.

In the past 5 years, the growing industry interest motivated new studies on quantifying the fatigue-fracture resistance of the relatively brittle high-strength reinforcement [13]. Slavin and Ghannoum [14] conducted the experimental study on the low-cycle fatigue resistance of three steel grades (Gr 60, Gr 80, and Gr 100) with three different bar sizes (#5, #8, and #11) from two manufacturing procedures. The average fatigue lives of Gr 80 and 100 reinforcing bars were found to be shorter than but still comparable to the average fatigue life of Grade 60 bars. Meanwhile, large variations were seen between different batches and different manufacturing procedures. The experimental observation also indicated that bar buckling can shorten the fatigue life of reinforcement. Moreover, the bar ruptures were typically observed in one to two cycles after the major crack formed.

Driven by the objective to simulate reinforcement fracture under earthquake loads and its consequent impacts on the reinforced concrete structures, this paper introduces the development, validation and application of a new reinforcement ductile fracture model. First, the state-of-the-art fatigue-fracture method is briefly reviewed, and its limitations are discussed. Then, the formulation of the new fracture model is introduced. In this study, the new model is also implanted in OpenSees [15] as a new uniaxial-material module. The modeling approach using the new material in the fiber element analysis is introduced. Numerical simulation for a recent shake-table bridge column test is presented to validate the use of the new fracture model for simulating observed bar ruptures in the test. Last but not lease, one archetype single-bent-column bridge is modeled and analyzed using the calibrated fiber analysis approach with the new fracture material. Analysis results are introduced to (1) demonstrate the importance of simulating the reinforcement bar fracture for assessing the seismic performance of reinforced concrete bridge columns; and (2) the efficacy of the new ductile fracture model and the new uniaxial material.

2. Review of the State-of-the-Art Method

In this paper, the state-of-the-art method for predicting reinforcement fatigue-fracture refers to the empirical strain-based mathematical model that is calibrated to available data on bare bar tests. For instance, in the authors' preceding study [16], the parametric fatigue-fracture model, as shown in Eq. (1), was derived from the classical Coffin-Manson model. The three modeling coefficients (α_f, C_f, and ε_f) were calibrated for different types of reinforcement. Predictive equations were also developed for estimating the modeling coefficients based on the basic reinforcement properties, i.e., yield strength f_y, young's modulus E_s, tensile-to-yield strength ratio T/Y, bar diameter d_b, and bar slenderness ratio s/d_b.

$$FI = \sum_{i=1}^{N} \left(\varepsilon_{pi} / C_f \right)^{1/\alpha_f} \tag{1}$$

$$\begin{cases} \alpha_f = 0.080 - 0.045 \cdot \left(f_y / 60ksi \right) + 0.027 \cdot \left(s/d_b \right) + 0.129 \cdot \left(T/Y \right) \\ C_f = 0.5^{\alpha_f} \cdot \left(\varepsilon_f - f_y / E_s \right) \\ \varepsilon_f = f_y / E_s - 0.043 \cdot \left(f_y / 60ksi \right) + 0.128 \cdot \left(T/Y \right) + 0.018 \cdot \left(d_b / 1in \right) \end{cases} \tag{2}$$

For any specific random reinforcement strain history, the equivalent half-cycle plastic strain amplitudes would be computed by the rain-flow counting algorithm. The reinforcement properties would be used to compute the modeling coefficients. The resulting fracture index (*FI*) can be computed by substituting the counted equivalent plastic strain amplitudes and the modeling coefficients into Eq. (1). Based on the statistics of computed *FIs* for 206 bar bare tests [14], the median value of *FIs* at observed bar rupture points is 1.0. The advantages of this kind of empirical models include: (1) the capability of capturing the differences in different steel grades; (2) the use of T/Y as the proxy of different manufacturing processes; and (3) the consideration of buckling effects on fatigue resistance by including s/d_b in predictive equations. These features help to efficiently quantify the bar fracture probability in the post-processing stage and help to develop effective design strategies to mitigate buckling effects.

However, several limitations are also noticed by the authors. The first constraint is the assumption inherited from the classical Coffin-Manson model: the half-cycle number before the failure is a linear function of the plastic strain amplitude in the log-log scale. This assumption was initially proposed for the small coupon tests where the bar buckling is excluded. As will be discussed later, in the cyclic bare bar tests and under the real earthquake loads, the bar buckling can cause the strain localization which is dependent on the loading history and may not conformed to the log-log linear assumption. The second limitation is the empirical model does not consider the strain concentration after the bar necking. Therefore, its accuracy under large strain amplitudes is replied on the linear extrapolation of the model. Furthermore, although the rain-flow counting is developed and frequently used for high-cycle and low-cycle fatigue problem, there is few studies validating its usage for ultra-low cycle problems. Meanwhile, it is difficult to adapt the rain-flow counting algorithm in real-time simulation without introducing simplifications and errors.

3. New Reinforcement Ductile Fracture Model

The proposed reinforcement ductile fracture model is established on preceding research thrusts to simulate ductile fracture of engineering steel materials [17-22]. As expressed in Eq. (3), the real-time damage is quantified by the fracture index *FI*, which is dependent on the strain history (Fig. 1a) and the stress triaxiality history (Fig. 1b) characterized at the fracture loci. The fracture failure is predicted when the evaluated *FI* reaches 1.0 (e.g., the solid curve in Fig. 1c).

$$FI = Ce^{\lambda \int_{T<0} d\varepsilon_p} \int \left(\beta e^{A^+ T} - e^{-A^- T} \right) d\varepsilon_p \tag{3}$$

where, C is void-growth constant; λ and β are cyclic deterioration coefficient and symmetry coefficient; A and A- are triaxiality coefficients for tension and compression cycles, respectively, which are taken as 1.3

[21, 22]; T is stress triaxiality as the ratio of hydrostatic stress σ_m and effective stress σ_e, i.e., T = σ_m/σ_e, and in reinforcement under axial loads, T is positive under tension and negative under compression; and $d\varepsilon_p$ is absolute incremental plastic strain at the fracture loci.

$$\begin{cases} \beta = 1.0 + (\beta_0 - 1.0)\left[\dfrac{\min(\Delta\varepsilon_{\max}, \Delta\varepsilon_{th})}{\Delta\varepsilon_{th}}\right]^{\gamma} \\ \lambda = \lambda_0\left[\dfrac{\min(\Delta\varepsilon_{\max}, \Delta\varepsilon_{th})}{\Delta\varepsilon_{th}}\right]^{\gamma} \end{cases} \tag{4}$$

where, β_0 and λ_0 are material constants to be calibrated; $\Delta\varepsilon_{max}$ is the absolute difference between the minimum and maximum strains; $\Delta\varepsilon_{th}$ is the threshold strain range that is take as 0.05 in this study; and γ is taken as 1.0.

Following the well-established ductile fracture mechanisms, the material failure under cyclic loads is attributed to two major damage processes: (1) the void growth under hydrostatic tension and shrinkage under hydrostatic compression [23]; and (2) the capacity degradation due to geometric (e.g., nonuniform void deformation or buckling) and material (e.g., degradation of the inter-void ligament) factors [21]. In the proposed model, the first damage process is tracked by the cyclic void-growth term (e.g., the dashed curve in Fig. 1c). The second damage process is measured by the cyclic deterioration term (e.g., the dotted curve in Fig. 1c), which only decreases under compressive loads. The materials with larger C or larger β_0 are more vulnerable to the void growth damage and their failure would usually be earlier under the same loading protocol (Fig. 1d and 1e). The materials with larger λ_0 would have faster capacity deterioration; and thus, the would also be less ductile under cyclic loads (Fig. 1f).

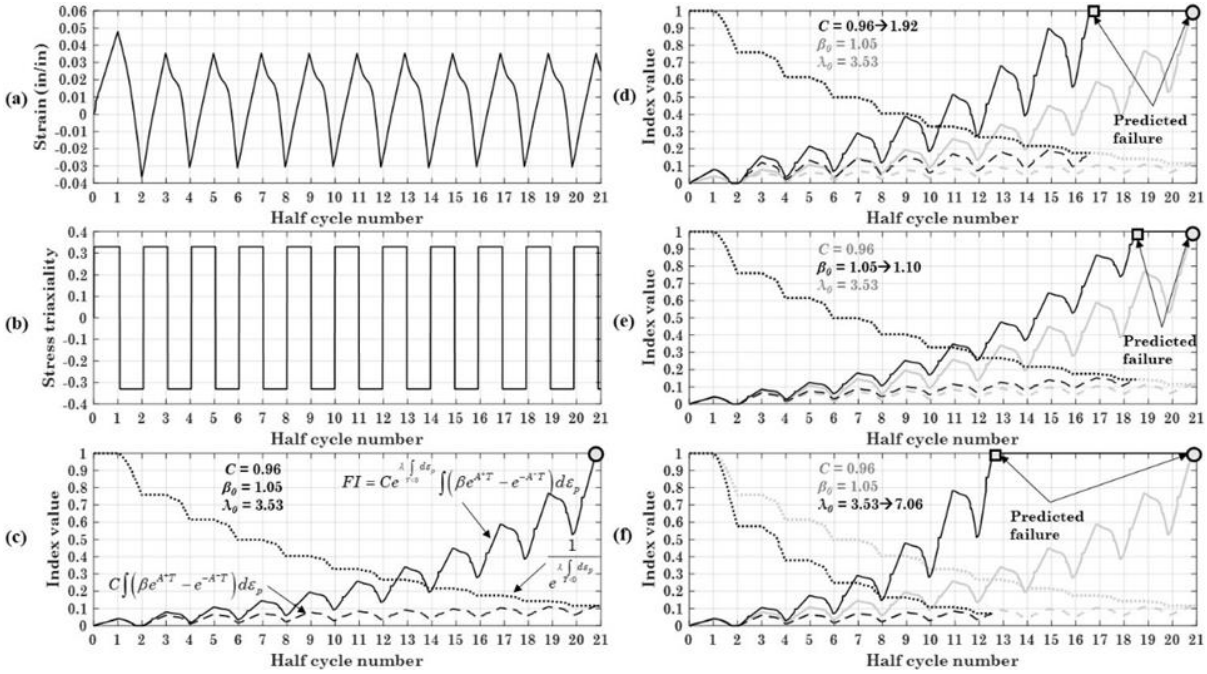

Fig. 1 – (a) Sample local strain history. (b) Sample stress triaxiality history. (c) Fracture index (*FI*) history and its two components, the cyclic void growth term and the capacity deterioration term. (d) Effect of the void-growth coefficient. (e) Effect of the symmetry coefficient. (f) Effect of the cyclic deterioration coefficient.

The key difference between the state-of-the-art method and the new fracture model is that the local strain, instead of the gauge strain, is used to indicate fracture failure in the new fracture model. Fig. 2 illustrates the calibration process of one #11 Grade 60 bare bar test under cyclic constant-amplitude loads.

The detailed fiber element is built in OpenSees (Fig. 2a) and analyzed under the testing loading protocol. The basic steel constitutive model is calibrated such that the simulated gauge strain-stress response matches the test result (Fig. 2b). The local strain histories at extreme locations (at the mid-span) in the buckled bar are recorded (Fig. 2c). The modeling coefficients are calibrated such that the *FI* of the most critical fiber in the specimen (usually at the compressive side of the mid-span section) equals 1.0 at the reported fracture point.

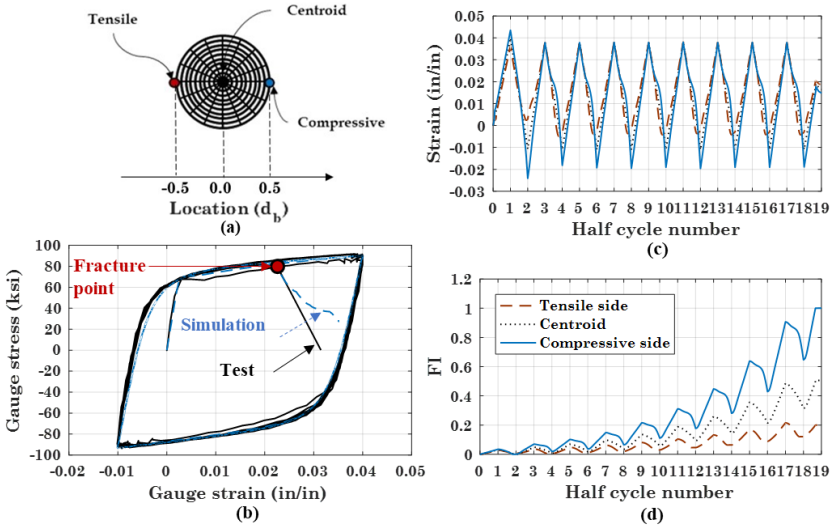

Fig. 2 – Strain and fracture index histories at different locations (#11 Gr. 60 bar with s/d_b = 4 under -1%~4% cyclic loads which failed during the 19th half cycle). The calibrated modeling coefficients: C = 0.92, λ_0 = 5.71, β_0 = 1.05. (a) Bar cross-section view. (b) Gauge strain-stress data in test and simulation. (c) Local strain histories at three extreme locations. (d) *FI* histories at three extreme locations.

This calibration process decouples the damage due to the buckling-induced strain localization and the damage due to cumulative strain cycles. The calibrated modeling coefficients should ideally be the same for a specific reinforcing steel material and should be independent with the bar slenderness and the loading history. In the commonly used fiber element analyses for concrete members, one reinforcement is usually modeled with one single fiber on each cross section whose material behavior is defined by a uniaxial material. The uniaxial material only has 1D strain-stress responses which are essentially the gauge strain-stress responses over the corresponding integration length. In order to apply the developed fracture model, which is calibrated to local strain demands, to fiber element analyses, the closed-form solution for local strain demands after bar buckling is also developed. As shown in Eq. (3), the critical local strain is computed by subtracting the buckling-induced strain concentration from the gauge strain. The buckling-induced strain concentration is the product of the bar radius ($d_b/2$) and the equivalent curvature (ϕ^*) which is defined as a function of the current gauge strain range ($\Delta\varepsilon_{gauge}$), and two modeling coefficients (b_1 and b_2). Fig. 3 shows one example of the calibrated closed-form solution for the equivalent curvature of the #8 Grade 100 reinforcement with slenderness ratio of 6.

$$\varepsilon_{local} = \varepsilon_{gauge} - \phi^* \cdot \left(\frac{d_b}{2}\right) = \varepsilon_{gauge} - b_1 \sinh\left(\frac{\Delta\varepsilon_{gauge}}{b_2}\right) \cdot \left(\frac{d_b}{2}\right) \quad (3)$$

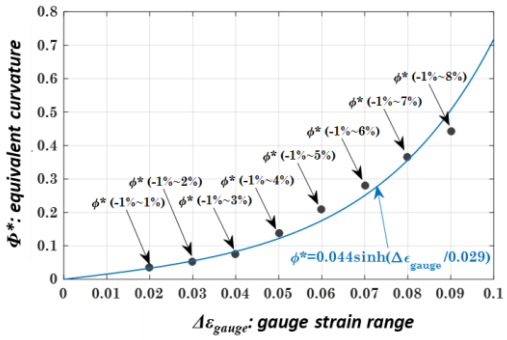

Fig. 3 – Calibrated equivalent curvature ϕ^* model (#8 Grade 100 reinforcement s/d_b = 6).

Following the similar idea, the closed-form solution for local strain and triaxiality demands after bar necking is also developed. As expressed in Eq. (4) and Eq. (5), the local strain and triaxiality are assumed as the piece-wise linear functions of the gauge strain amplitude (ε_{gauge}) with two modeling coefficients (k_1 and k_2). Fig. 4 shows one example of the calibrated closed-form solution of the #5 Grade 60 reinforcement.

$$\varepsilon_{local} = \begin{cases} \varepsilon_{gauge}, & \varepsilon_{gauge} \le \varepsilon_{su} \\ \varepsilon_{su} + k_1\left(\varepsilon_{gauge} - \varepsilon_{su}\right)\left(\dfrac{L_{gauge}}{8\ in.}\right), & \varepsilon_{gauge} > \varepsilon_{su} \end{cases}, \quad k_1 = \frac{\varepsilon_{f,local} - \varepsilon_{su}}{\varepsilon_{f,gauge} - \varepsilon_{su}}. \tag{4}$$

$$|T| = \begin{cases} 0.33, & \varepsilon_{gauge} \le \varepsilon_{su} \\ 0.33 + k_2\left(\varepsilon_{gauge} - \varepsilon_{su}\right)\left(\dfrac{L_{gauge}}{8\ in.}\right), & \varepsilon_{gauge} > \varepsilon_{su} \end{cases}, \quad k_2 = \frac{T_f - 0.33}{\varepsilon_{f,gauge} - \varepsilon_{su}}. \tag{5}$$

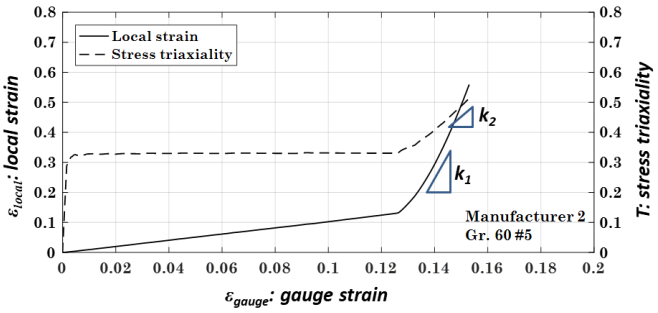

Fig. 4 – Calibrated closed-form solution for necking-induced strain amplification (k_1 = 8.67, k_2 = 3.45, #5 Grade 60 reinforcement).

4. Validation: Shake-Table Bridge Column Test

To facilitate the use of the proposed reinforcement ductile fracture model in the fiber element analysis, a new uniaxial material is coded and implanted into OpenSees. The modeling command is: uniaxialMaterial DuctileFracture $matTag $refTag -c_mono $c_mono -c_cycl $c_cycl -c_symm $c_symm <-E_s $E_s> <-esu $esu –k1 $k1 -k2 $k2> <-db $db –b1 $b1 –b2 $b2>, where $matTag is the current material tag; $refTag is the material tag of steel material; $c_mono, $c_cycl, and $c_symm are the three modeling coefficients C, λ_0, and β_0, respectively; $E_s is the Young's modulus; $esu is the uniform strain; $k1 and $k2 are the two modeling coefficients for necking-induced strain concentration; $db is the bar diameter; and $b1 and $b2 are two modeling coefficients for buckling-induced strain localization.

The validation study for this new OpenSees material is presented hereafter. The fiber element analysis is conducted in OpenSees to simulate a recent shake-table test of a bridge column [24]. The column design was conformed to the minimum requirements of AASHTO [25]. The height of column was 72 in; the diameter was 16 in; the axial load ratio was 8%; and the concrete clear cover was 0.75 in. The column cross section was designed with 22 #4 Grade 60 bars; and the core concrete was confined by #3 Grade 60 bars with a 1.5 in. tie spacing in the plastic hinge region. One main-shock and one after-shock ground motions from the 2011 Tohoku Earthquake were selected and adapted in the experiment. The column was tested under three 1D ground motion records in sequence: (1) 100% main shock, (2) 100% after shock; and (3) 125% main shock.

As shown in Fig. 5, the bridge column is modeled as a force-based fiber element with 6 Gauss-Labotto integration points and a zero-length section element using Bond_SP01 material [26] for bar-slip responses. The column cap and base-block are explicitly modeled as rigid-link element. Overall 80 ksi axial load is applied and maintained during simulation at the top of the column model. The mass corresponding to 80 ksi force is assigned to Node 5. All material parameters are adopted from the measured values in the experiment [24]. The seven modeling coefficients in ductile fracture model are: C = 1.77, λ_0 = 0.92, β_0 = 1.02, k_1 = 13.2, k_2 = 5.97, b_1 = 0.051, and b_2 = 0.047. Fig. 6(a) shows the simulated hysteresis compared with the test hysteresis. The red dots in Fig. 6 refer to 3 simulated bar ruptures, which is consistent with the total number of fractured bars in the experiment. Fig. 6(b) shows the simulated fracture index histories of 22 bars in analysis. The first simulated bar rupture occurs at the test time of 443 sec, which is very close to the reported fracture time at 430 sec in the experiment.

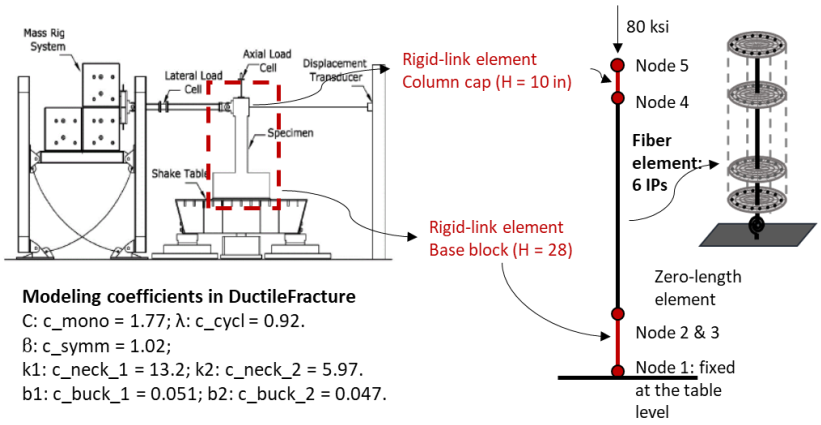

Fig. 5 – Calibrated fiber element analysis for simulating the bar ruptures observed in the shake-table test.

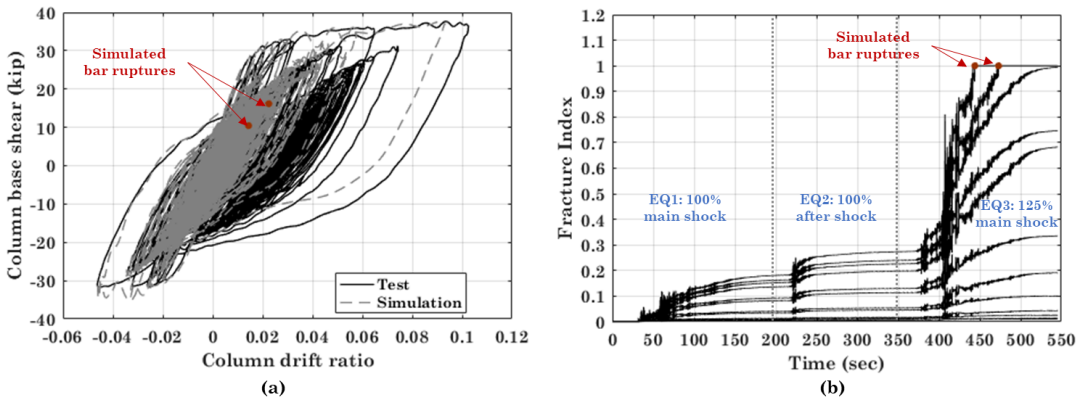

Fig. 6 – (a) Test and simulated column base shear and column drift ratio. (b) Fracture index histories of individual reinforcement in analysis.

5. Application: Bar Fracture Simulation and Bridge Collapse Assessment

This section presents the case study to demonstrate the application of the proposed fracture model in evaluating the steel bar fracture fragility and collapse risk of concrete bridge columns. One archetype singe-column-bent bridge is examined in this study. Its two spans have the same length of 100 ft; the column clear height is 24 ft; the column diameter is 60 in; and the design axial load is 8% of the nominal axial load capacity of the column. The column cross section is designed with concrete strength of 4 ksi and 36 #11 Grade 60 longitudinal bars; and the core concrete is confined by #8 Grade 60 hoops with the tie spacing of 8.4 in ($6d_b$). The design is conformed to the Caltrans Seismic Design Criteria [27] and AASTHO specification [25].

As show in Fig. 7, the numerical model is built for the entire bridge system in OpenSees. The foundation responses are modeled by two condensed rotational hinges at the column base whose properties are based on the detailed fiber element analysis of the pile foundation under combined vertical and lateral loads. The shear keys are modeled by hysteretic hinges following the study by Bozorgzadeh et al. [28]. The Abutment responses are modeled by the hyperbolic gap springs following the study by Aviram et al. [29]. The bearings are modeled using 3D elastomeric bearing elements with material properties suggested by the study by Roeder and Stanton [30]. The superstructure is modeled by the elastic beam-column elements. The column is modeled by one force-based fiber element with 6 Gauss-Labotto integration points. Two 3D zero-length section elements are used at the two ends of the column to capture the bond slip responses. The Bond_SP01 material is used to define the reinforcement material in the bond slip elements with modeling coefficients: S_y = 0.06 in, S_u = 2.05 in, b_s = 0.3, and R = 0.5. The new DuctileFracture material is used to define the reinforcement material in the column fiber element with modeling coefficients: C = 1.93, λ_0 = 2.42, β_0 = 1.02, k_1 = 6.64, k_2 = 3.49, b_1 = 0.05, and b_2 = 0.03.

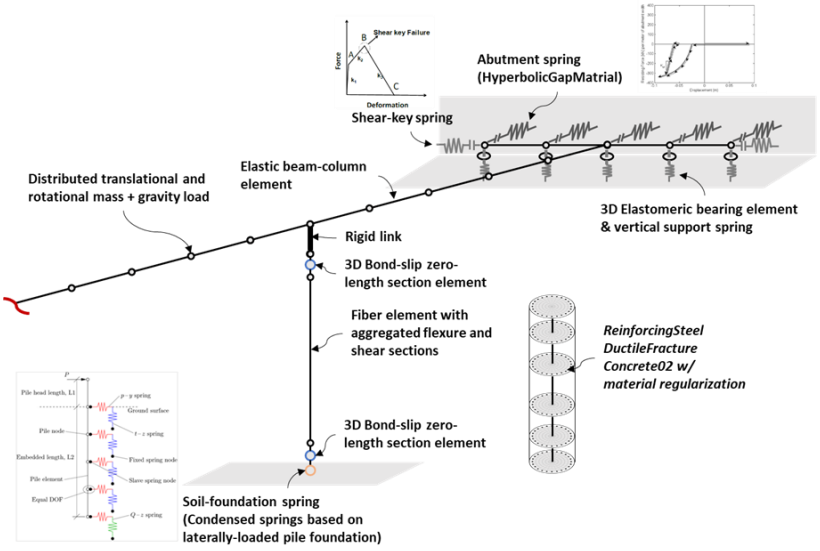

Fig. 7 – Sketch plot of the numerical OpenSees model for the archetype bridge system.

The incremental dynamic analysis is conducted to evaluate the seismic performance of the archetype bridge system. In the preceding study on the ground motion duration effects on the structural collapse performance [31], two supplementary intensity measures were found to influence the structural collapse capacity: SaRatio($0.2T_1$,T_1,$3T_1$) and $Ds_{5\text{-}75}$, where T_1 is the conditional period selected for the structure. For the archetype bridge system in this study, T_1 is taken as 1.0s. Overall 49 ground motion records are selected from available strong motion databases (NGA-West2 [32] and CESMD [33]) such that their SaRatio(0.2s,1s,3s)'s and $Ds_{5\text{-}75}$'s cover a wide range of different combinations, as shown in Fig. 8(a). Fig. 8(b) shows the unscaled response spectra of the 49 selected records.

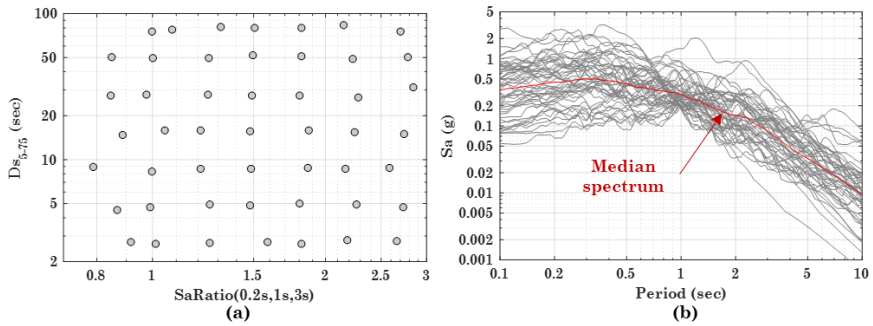

Fig. 8 – (a) SaRatio(0.2s,1s,3s) and Ds_{5-75} of ground motion records that are used in IDA. (b) Response spectra (5% damping ratio) of unscaled ground motion records that are used in IDA.

The incremental dynamic analysis is conducted for the archetype bridge column under each of these 49 ground motion records until the collapse occurs, which is defined by the maximum curvature ductility factor (μ_ϕ) in analysis exceeding 50. In order to illustrate the importance of simulating the bar rupture failure in analysis, the analysis is also conducted for the same numerical model but without explicitly modeling bar fracture using the DuctileFracture material. Fig. 9 compares the simulated column responses under one ground motion record from these two modeling approaches. Referring to Fig. 9(a), because of the concessive bar ruptures is captured, the column shear strength degraded in the analysis with the DuctileFracture material; whereas, there is no significant strength drop in the analysis without the DuctileFracture material. Similar to the observation in Fig. 9(a), Fig. 9(b) indicates that the DuctileFracture material can simulate the column stiffness degradation after bar ruptures; and thus, the analysis captures more intense curvature demands than the curvature demands in the analysis without using the DuctileFracture material.

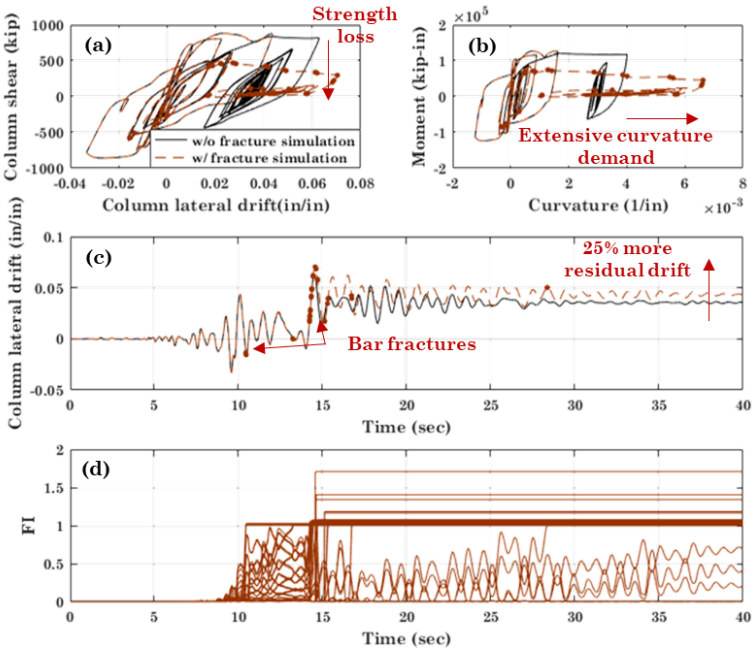

Fig. 9 – Comparison between simulated structural responses with and without simulating the bar ruptures in analysis. (a) Hysteresis (column shear versus lateral drift ratio). (b) Moment-curvature responses at the column base. (c) Time histories of column lateral drift ratio. (d) Fracture index (*FI*) time histories of individual reinforcing bars.

Following the preceding study on developing analytical fragility functions for bridge components [34-36], the component damage threshold (CDT) metrics are used to classify the bridge damage states in this

study. The four damage states (indicated by CDT-0 to CDT-3) are determined by the maximum μ_ϕ in the analysis exceeding 1.0, 5.0, 11.0, and, 17.5 respectively; and they refer to (1) cracking; (2) minor covering spalling at the top and bottom of the column; (3) major spalling, exposed core, or confinement yield; and (4) loss of confinement, longitudinal bar buckling or rupture, core crushing, or large residual drift. Fig. 10(a) shows the resulting analytical fragility functions without simulating the bar fracture, where the median Sa's for the four damage states are 0.49g, 0.81g, 1.29g, and 1.78g, respectively. Fig. 10(b) shows the same fragility functions if simulating the bar fracture in analysis: the median Sa's for CDT-0 and CDT-1 are found to be similar to the results in Fig. 10(a); whereas, the median Sa for CDT-2 is decreases by about 10% and the median Sa for CDT-3 decreases by about 23%. Fig. 10(c) also contrasts the collapse fragility functions with and without simulating the bar fracture in analysis. Similar to the findings for the CDT-2 and CDT-3 damage states, the analysis without considering bar fracture failure could overestimate the median collapse capacity.

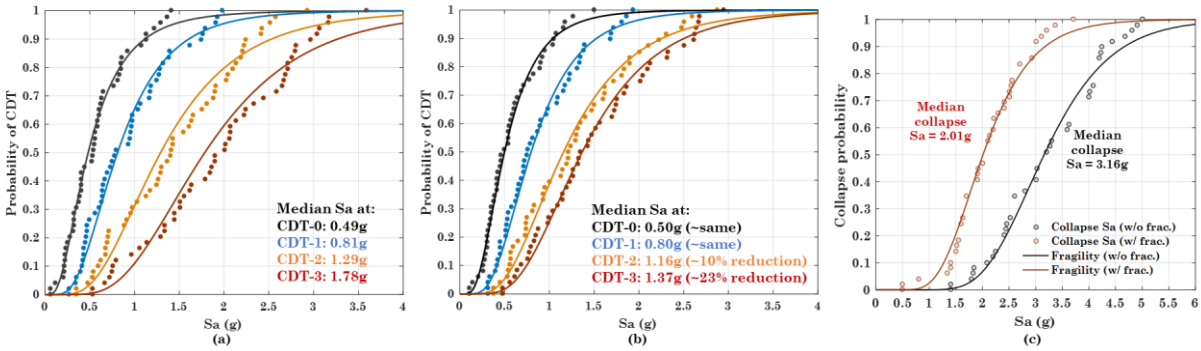

Fig. 10 – (a) Fragilities of four bridge column damage states without simulating bar fracture by DuctileFracture. (b) Fragilities of four bridge column damage states using DuctileFracture. (b) Comparison of the collapse fragilities.

6. Summary

In this paper, the state-of-the-art fatigue-fracture method is briefly reviewed, and its limitations are discussed. Then, the formulation of the new ductile fracture model is introduced. The proposed model quantifies the cumulative damage by the fracture index (*FI*) which is computed from the plastic strain and stress triaxiality history at the fracture loci. The calibration process for three modeling coefficients () is demonstrated. Two closed-form solutions for local strain demands with necking-induced and buckling induced strain localizations are developed. The proposed model is implanted in OpenSees as a new uniaxial material. Then, the validation study is presented in which the observed reinforcement ruptures in one shake-table bridge column test can be accurately simulated by using the new uniaxial material in the fiber element analysis. Last but not least, the case study is also presented to (1) the efficacy of the new ductile fracture model and the new uniaxial material to simulate the stiffness degradation and strength loss of reinforced concrete members due to reinforcement fracture; and (2) demonstrate the importance of simulating the reinforcement bar fracture for assessing the seismic performance of reinforced concrete bridge columns, i.e., to avoid the estimation bias in the analysis without considering bar fracture where the median collapse capacity is significantly overestimate.

7. Acknowledgements

This research is supported by the PEER – TSRP (S2), the Charles Pankow Foundation, and the Blume Center for Earthquake Engineering. The authors gratefully acknowledge Mojtaba Alian, Mohammed Moustafa, and David Sanders for sharing their findings in the companion PEER project, and to researchers associated with ACI HS reinforcement working group: Wassim Ghannoum, Andres Lepage, Dominic Kelly, and Jack

Moehle for sharing their knowledge and test data. Computing resources were provided by the Blume Earthquake Engineering Center and Sherlock computing cluster at Stanford University.

8. Copyrights

9. References

[1] Palmgren, A. (1924). Durability of ball bearings. ZVDI, 68(14), 339-341.

[2] Miner, M. A. (1945). Cumulative fatigue damage. Journal of applied mechanics, 12(3), A159-A164.

[3] Manson, S. S. (1953). Behavior of materials under conditions of thermal stress (Vol. 2933). National Advisory Committee for Aeronautics.

[4] Coffin Jr, L. F. (1954). A study of the effects of cyclic thermal stresses on a ductile metal. Transactions of the American Society of Mechanical Engineers, New York, 76, 931-950.

[5] Smith, R. W., Hirschberg, M. H., & Manson, S. S. (1963). Fatigue behavior of materials under strain cycling in low and intermediate life range (No. NASA-E-TN-D-1574). NATIONAL AERONAUTICS AND SPACE ADMINISTRATION CLEVELAND OH LEWIS RESEARCH CENTER.

[6] Coffin, L. (1962). Experimental Support for Generalized Equation Predicting Low Cycle Fatigue. Journal of Basic Engineering, Trans. ASME (Series D), 533-537.

[7] Smith, K. (1970). A stress-strain function for the fatigue of metals. Journal of materials, 5, 767-778.

[8] Koh, S. K., & Stephens, R. I. (1991). Mean stress effects on low cycle fatigue for a high strength steel. Fatigue & Fracture of Engineering Materials & Structures, 14(4), 413-428.

[9] Downing, S. D., & Socie, D. F. (1982). Simple rainflow counting algorithms. International journal of fatigue, 4(1), 31-40.

[10] Rychlik, I. (1987). A new definition of the rainflow cycle counting method. International journal of fatigue, 9(2), 119-121.

[11] Mander, J. B., Panthaki, F. D., & Kasalanati, A. (1994). Low-cycle fatigue behavior of reinforcing steel. Journal of Materials in Civil Engineering, 6(4), 453-468.

[12] Brown, J., & Kunnath, S. K. (2004). Low-cycle fatigue failure of reinforcing steel bars. Materials Journal, 101(6), 457-466.

[13] Kelly, D. J., Lepage, A., Mar, D., Restrepo, J. I., Sanders, J. C., & Taylor, A. W. (2014, July). Use of high-strength reinforcement for earthquake-resistant concrete structures. In Tenth US National Conference on Earthquake Engineering, Anchorage, AK (pp. 21-25).

[14] Ghannoum, W. M., & Slavin, C. M. (2016). Low-cycle fatigue performance of high-strength steel reinforcing bars. ACI Materials Journal, 113(6), 803.

[15] McKenna, F. (2011). OpenSees: a framework for earthquake engineering simulation. Computing in Science & Engineering, 13(4), 58-66.

[16] Zhong, K., Deierlein, G. G. (2019) Low-Cycle Fatigue Effects on the Seismic Performance of Concrete Frame and Wall Systems with High Strength Reinforcing Steel[R]. Charles Pankow Foundation.

[17] Kanvinde, A. M., & Deierlein, G. G. (2007). Finite-element simulation of ductile fracture in reduced section pull-plates using micromechanics-based fracture models. Journal of Structural Engineering, 133(5), 656-664.

[18] Kanvinde, A. M., & Deierlein, G. G. (2007). Cyclic void growth model to assess ductile fracture initiation in structural steels due to ultra low cycle fatigue. Journal of engineering mechanics, 133(6), 701-712.

[19] Fell, B. V., Kanvinde, A. M., Deierlein, G. G., & Myers, A. T. (2009). Experimental investigation of inelastic cyclic buckling and fracture of steel braces. Journal of structural engineering, 135(1), 19-32.

[20] Myers, A. T., Kanvinde, A. M., & Deierlein, G. G. (2010). Calibration of the SMCS criterion for ductile fracture in steels: specimen size dependence and parameter assessment. Journal of engineering mechanics, 136(11), 1401-1410.

[21] Smith, C., Kanvinde, A., & Deierlein, G. (2017). A local criterion for ductile fracture under low-triaxiality axisymmetric stress states. Engineering Fracture Mechanics, 169, 321-335.

[22] Terashima M., Deierlein G. G. & Kanvinde A. (2018). Computational Simulation of Ductile Fracture in Buckling Restrained Braces. Proceedings of the 11th National Conference in Earthquake Engineering, Earthquake Engineering Research Institute, Los Angeles, CA. 2018.

[23] Rice, J. R., & Tracey, D. M. (1969). On the ductile enlargement of voids in triaxial stress fields∗. Journal of the Mechanics and Physics of Solids, 17(3), 201-217.

[24] Mohammed, M. S., Sanders, D., & Buckle, I. (2015). Shake Table Tests of Reinforced Concrete Bridge Columns Under Long Duration Ground Motions. In 6th International Conference on Advances in Experimental Structural Engineering.

[25] American Association of State Highway and Transportation Officials. (2014). AASHTO LRFD bridge design specifications. Washington, D.C.

[26] Zhao, J., & Sritharan, S. (2007). Modeling of strain penetration effects in fiber-based analysis of reinforced concrete structures. ACI structural journal, 104(2), 133.

[27] Caltrans, S. D. C. (2019). Caltrans seismic design criteria. California Department of Transportation, Sacramento, CA.

[28] Bozorgzadeh, A., Megally, S., Restrepo, J. I., & Ashford, S. A. (2006). Capacity evaluation of exterior sacrificial shear keys of bridge abutments. Journal of Bridge Engineering, 11(5), 555-565.

[29] Aviram, A., Mackie, K. R., & Stojadinovic, B. (2008). Effect of abutment modeling on the seismic response of bridge structures. Earthquake Engineering and Engineering Vibration, 7(4), 395-402.

[30] Roeder, C. W., & Stanton, J. F. (1991). State-of-the-art elastomeric bridge bearing design. Structural Journal, 88(1), 31-41.

[31] Chandramohan, R., Baker, J. W., & Deierlein, G. G. (2016). Impact of hazard-consistent ground motion duration in structural collapse risk assessment. Earthquake Engineering & Structural Dynamics, 45(8), 1357-1379.

[32] Ancheta, T. D., Darragh, R. B., Stewart, J. P., Seyhan, E., Silva, W. J., Chiou, B. S. J., ... & Kishida, T. (2014). NGA-West2 database. Earthquake Spectra, 30(3), 989-1005.

[33] Haddadi, H., Shakal, A., Stephens, C., Savage, W., Huang, M., Leith, W., ... & Borcherdt, R. (2008, January). Center for engineering strong-motion data (CESMD). In Proceedings of the 14th World Conference on Earthquake Engineering, Beijing, October (pp. 12-17).

[34] Padgett, J. E., & DesRoches, R. (2008). Methodology for the development of analytical fragility curves for retrofitted bridges. Earthquake Engineering & Structural Dynamics, 37(8), 1157-1174.

[35] Ramanathan, K. N. (2012). Next generation seismic fragility curves for California bridges incorporating the evolution in seismic design philosophy (Doctoral dissertation, Georgia Institute of Technology).

[36] Mangalathu, S. (2017). Performance based grouping and fragility analysis of box-girder bridges in California. Georgia Institute of Technology.

